Electrochimica Acta 536 (2025) 146806

Contents lists available at ScienceDirect

Electrochimica Acta

journal homepage: www.journals.elsevier.com/electrochimica-acta

New design high energy density Li-ion battery based on self-standing electrodes configuration

Luca Minnetti [a,b,*], Leonardo Sbrascini [a], Asia Patriarchi [a], Antunes Staffolani [a,c], Maddalena Barcaioni [a,b], Luca Bottoni [a], Francesco Nobili [a,b]

[a] School of Sciences and Technologies – Chemistry Division, University of Camerino, Via Madonna delle Carceri ChIP, 62032, Camerino, Italy
[b] National Reference Center for Electrochemical Energy Storage (GISEL) – INSTM, Via G. Giusti 9, 50121, Firenze, Italy
[c] University of Bologna, Department of Chemistry "Giacomo Ciamician", UE4 – Via Piero Gobetti 85, 40129, Bologna, Italy

ARTICLE INFO

Keywords:
Self-Standing
Free-Standing
Li-ion
Energy Density
LFP

ABSTRACT

The utilization of lithium-ion batteries (LIBs) is currently pervasive as high-performance energy storage technology. While graphite anode and $LiFePO_4$ (LFP) cathode can be regarded as a baseline for improvements in the field of materials, their utilization is now revamping at production level, mainly because of their cost, safety and acceptable performances. In this context, many different approaches have already been explored to boost cell performance by optimizing its design. Nevertheless, further improvements can still be achieved to make commercial batteries more performing and reduce the costs, such as optimization of current collectors design. In this regard, an easy coating technique is applied to produce self-standing electrodes of both Graphite and LFP with high areal loadings, demonstrating their application in a Li-ion full cell with improved energy density. Both electrodes are first tested in lithium half-cells, displaying suitable interfacial and ion transport properties and good cycling performance and capacity retention. Furthermore, coin-type full cell delivers good cycling performance and excellent coulombic efficiency at C/3, with a limited capacity fade over 300 cycles and an initial energy density of about 240 Wh Kg_{an+cat}^{-1}. Moreover, the self-standing electrodes are used in single-layer pouch (SLP) cell format, showing promising results for possible upscaling, despite further optimization are needed. The obtained results ultimately lead to the possibility of using this electrode design to further decrease cost and weight of commercial batteries, especially for application in electronic devices, increasing at the same time the achievable energy density.

1. Introduction

Nowadays Li-ion batteries (LIBs) are undoubtedly among the most used energy storage technologies for everyday life and have quickly become the preferred choice for application in electronic devices (i.e. smartphones, smartwatches, laptops) and in power electric vehicles (EVs), eventually aiming to a low-carbon society [1,2]. Despite the already established characteristics, there is still an increasing trend towards further improving specific energy densities to ensure higher driving ranges, due to political and economic advantages [3,4]. Several engineering techniques have been explored to maximize the energy density of the cells at the material level, either studying novel materials or modifying existing ones [5,6]. When it comes to electrode materials, graphite and $LiFePO_4$ (LFP) are considered as the state-of-the-art for the anode and cathode side of commercial batteries, respectively [7]. Indeed, bearing in mind economic aspects, they are among the cheapest solutions compared to other chemistries, especially when considering the cathode side, which accounts for a large part of the battery cost [3,8]. LFP possesses a flat voltage plateau at 3.5 V vs. Li^+/Li, with impressive thermal stability and a very stable structure upon prolonged charge/discharge cycling, which make this material highly attractive despite its relatively low energy density [9,10]. On the other hand, graphite has a very suitable structure for reversible intercalation of Li^+ ions without relevant volume expansion [11,12], which makes it a desirable material despite its lower intercalation capacity if compared to other systems such as Si-based anodes [13,14]. Hence, because of their safety, low cost, and established performance, the utilization of these commercial materials is not going to be abandoned soon at production level [15]. Nevertheless, they can be regarded as the baseline for further technological improvements. In this context, many approaches have

* Corresponding author.
E-mail address: luca.minnetti@unicam.it (L. Minnetti).

https://doi.org/10.1016/j.electacta.2025.146806
Received 24 March 2025; Received in revised form 13 June 2025; Accepted 29 June 2025
Available online 30 June 2025

been already explored in the literature to boost cell performances, which involve the optimization of electrode design parameters, such as porosity, electrode loadings, slurry composition and particle size [16–18]. Indeed, in the design of a Li-ion battery, the whole weight of the device plays an important role, and each component must be finely tuned to maximize the energy density [5,6]. This implies, for example, that an ideal electrode would be composed of a high active material loading (to increase capacity) and a thin current collector (to reduce inactive weight) [19].

The optimization of the current collector has also been the study object of some works, mainly focusing on surface modifications of the Cu/Al foils [20–22]. However, despite all the possible optimizations, the current collector itself remains as a "dead" weight inside the battery. In this regard, the production of self-standing electrodes would be an interesting approach to effectively reduce the weight of inactive components and enhance the cell energy density, although their fabrication poses several challenges on a large scale. Indeed, the preparation of self-standing (SS) electrodes has already been explored for analytical purposes, but either etching with acidic solutions or peeling with razor blades were necessary to perform the delamination of the active material from the current collector [23–26]. Moreover, in many cases the use of several plasticizers or other polymers is necessary in the production process to guarantee better mechanical properties, despite increasing the range of used materials and the costs involved in the fabrication [25,27,28]. In a more recent work, it was demonstrated that self-standing PVdF-based electrodes could be prepared via a versatile and cost-effective way, to produce "micro-reference" electrodes for EIS measurements [29]. The procedure simply involves coating the PVdF-based slurry onto a thin layer of commercial CMC (pre-coated on the chosen current collector), which can later be dissolved by water to delaminate the whole electrode coating.

In the present work, the latter approach was innovatively used to realize self-standing electrodes of commercial graphite and LFP (labelled as C6_SS and LFP_SS, respectively) with high mass loadings (i.e. ~7 mg cm^{-2} and ~ 11 mg cm^{-2}, respectively), with the aim to fabricate a functional Li-ion full cell with enhanced energy density. It is worth noting that this approach utilizes materials already present in the battery production supply chain, indicating easier input in the manufacturing process [30]. The produced self-standing electrodes were initially characterized in terms of structure and morphology by using X-ray diffraction (XRD) and scanning electron microscopy (SEM), and subsequently electrochemically evaluated in lithium half-cells by cyclic voltammetry (CV), electrochemical impedance spectroscopy (EIS) and galvanostatic cycling to assess their interfacial, ion transport and electrochemical properties. Subsequently, the electrodes have been coupled in a C6_SS|LFP_SS coin-type full cell to particularly investigate capacity retention, coulombic efficiency, and energy density, important parameters for application in relevant cell formats. In this regard, a proof-of-concept single-layer pouch (SLP) cell has been fabricated. The obtained results could possibly pave the way to the use of self-standing electrode design in commercial batteries with reduced costs and weight, coupled with enhanced energy density.

2. Experimental section

2.1. Preparation of self-standing electrodes

$LiFePO_4$ (LFP, Sigma-Aldrich) and graphite (KS15, Timcal) were chosen as cathode and anode, respectively, in order to prepare self-standing electrode with a procedure already reported in literature [29] (see photographic images of the different steps in **Figure S1**, Supporting Information). A 5 % wt solution of sodium carboxymethyl cellulose (CMC, Sigma-Aldrich, average molecular weight ~ 250000 g mol^{-1}) in water was prepared and cast by a doctor blade tool on copper foil (MTI Corp., thickness ~ 15 μm) and dried for 3 h on a hot plate at 90 °C to create a thin layer (see **Figure S1a**). The electrode slurries were obtained by dispersing the active material (either LFP or graphite), polyvinylidene fluoride (PVdF 5130 Solef®) binding polymer, carbon black (C65 carbon, Imerys) in 80:10:10 and 90:5:5 wt ratios for LFP and graphite, respectively, in N-methyl-2-pyrrolidone (NMP, Sigma-Aldrich). The slurries were stirred at room temperature until homogenization (about 3 h), and then cast by doctor blade over the CMC thin layer (**Figure S1b**). The obtained tapes were dried for 3 h on a hot plate at 70 °C, until complete NMP evaporation. After that, the coatings were immersed in water to dissolve the CMC layer until the complete detachment of the self-standing electrodes, labelled as C6_SS and LFP_SS for graphite and $LiFePO_4$, respectively (**Figure S1c-e**). The obtained self-standing coatings were dried to evaporate the excess of water (**Figure S1f**), cut into disks with diameter of 12 mm, and dried for 3 h at 120 °C under vacuum to remove possible residual traces of water and NMP solvent. The final active material loading ranged from 7 to 8 mg cm^{-2} for C6_SS and from 10 to 11 mg cm^{-2} for LFP_SS, as normalized to the electrode geometric area (1.13 cm^2).

2.2. Materials characterization and cell assembly

Scanning electron microscopy (SEM) images of LFP and graphite powders, LFP_SS and C6_SS samples were acquired by a Zeiss Sigma 300 field emission (FE-SEM) microscope. Energy dispersive X-ray spectroscopy (EDS) was performed on the SEM images through a X-ACT Cambridge Instruments analyzer. X-ray diffraction patterns (XRD) of powders and electrodes were collected using a Bruker D6 Phaser (40 kV, 15 mA) with non-monochromated Cu Kα radiation (λ = 1.5408 Å) and adopting a Si-strip SSD160–2 detector with 160 channels. Scans were performed in Bragg-Brentano mode in the 2θ range from 15° to 60° at a rate of 0.4 s $step^{-1}$ and a step size of 0.02°. CR2032 coin-type lithium half-cells (Hohsen Corporation) were assembled by using either LFP_SS or C6_SS 12 mm-diameter working electrodes and a 14 mm-diameter lithium metal disk as counter electrode, separated by a 16 mm-diameter glass fiber Whatman® GF/A disk. The CR2032 coin-type full cell was assembled by using a 12 mm-diameter LFP_SS cathode, a 12 mm-diameter C6_SS anode, and a 16 mm-diameter glass fiber Whatman® GF/A separator. A negative-to-positive (N/P) reversible capacity ratio of 1.1 was used. A 1 M solution of lithium hexafluorophosphate ($LiPF_6$) dissolved in a 1:1 (*v/v*) mixture of ethylene carbonate (EC) and dimethyl carbonate (DMC) (LP30, Solvionic, France) was used as electrolyte for all cells, which were assembled and sealed inside an Ar-filled glovebox (Jacomex GP Campus, O_2 and H_2O content lower than 1 ppm).

2.3. Electrochemical tests

The electrochemical process and the interphase characteristics of LFP_SS and C6_SS in lithium cell were investigated by cycling voltammetry (CV) and electrochemical impedance spectroscopy (EIS) at room temperature (T = 25°C). CR2032 Li|LFP_SS and Li|C6_SS coin cells were subjected to CV with a scan rate of 0.1 mV s^{-1} in the 2.5 – 4.2 V vs. Li^+/Li and 0.01 – 2.0 V vs. Li^+/Li potential ranges, respectively. EIS measurements were collected at the open circuit voltage (OCV) of fresh cells, and at bias potentials of 2.0 V and 2.5 V vs. Li^+/Li for C6_SS and LFP_SS, respectively, after 1, 5, and 10 CV cycles, by applying an alternate voltage signal of 10 mV in the 200 kHz – 100 mHz frequency range. The EIS spectra were analyzed via the non-linear least squares (NLLS) fitting method using the Equivalent Circuit software by Boukamp (only fits with χ^2 values of the order of 10^{-4} or lower were considered) [31,32]. Additional CV tests were performed within the same potential limits at scan rates of 0.05, 0.10, 0.15, and 0.20 mV s^{-1} to determine the Li^+ diffusion coefficients. Galvanostatic cycling tests were performed at room temperature (T = 25°C) to determine charge/discharge performances of Li|LFP_SS and Li|C6_SS CR2032 half-cells. Rate capability tests were performed by increasing the current rate from C/20 (1C = 170 mA g^{-1} for LFP_SS and 372 mA g^{-1} for C6_SS) to C/10, C/5, C/2 1C, 2C, 5C, then restoring the current rate to C/20, in the 2.5 – 4.2 V and 0.01 –

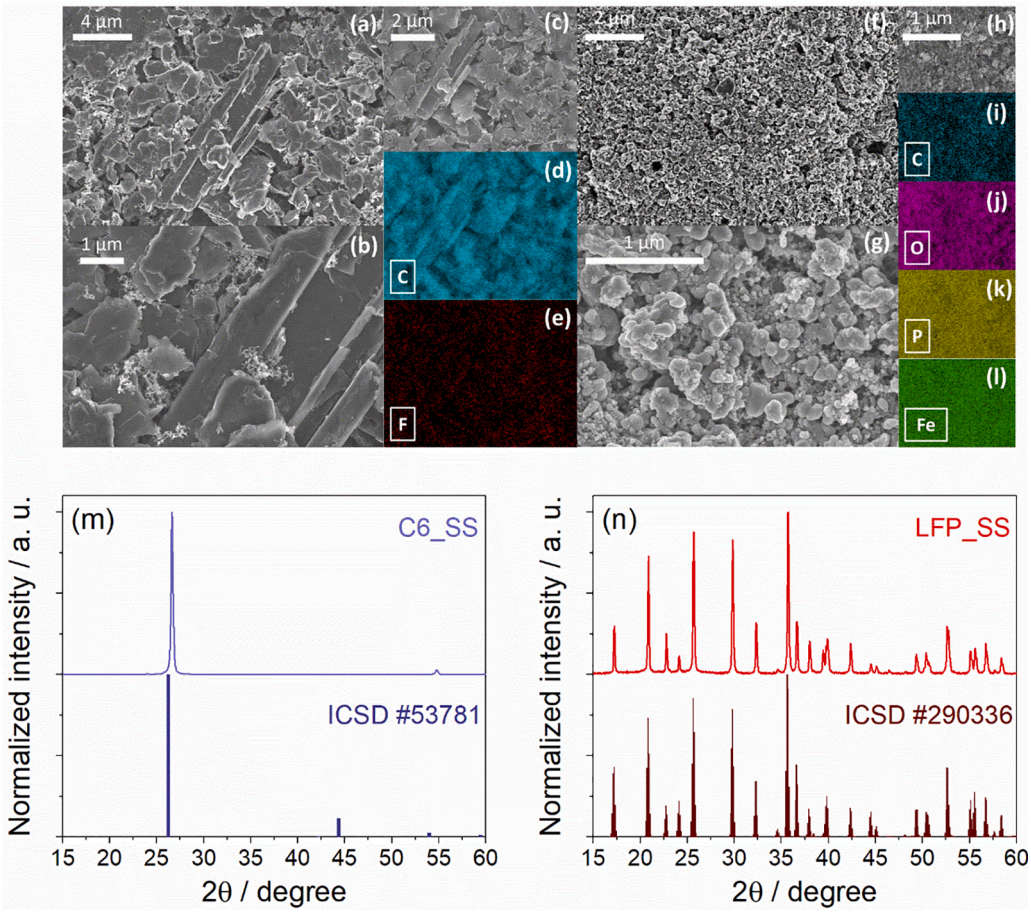

Fig. 1. SEM-EDS analysis of the (a-e) C6_SS and (f-l) LFP_SS. In detail: (a-c, f-h) SEM images at different magnifications and (d-e, i-l) corresponding EDS elemental maps of (d, i) C, (e) F, (j) O, (k) P, and (l) Fe. XRD patterns of (m) C6_SS and (n) LFP_SS compared to corresponding reference diffractograms (ICSD #53781 and ICSD #290336, respectively).

2.0 V voltage ranges for LFP_SS and C6_SS, respectively. Galvanostatic cycles at the C/3 rate were carried out for LFP_SS and for C6_SS within the same voltage ranges, after 2 activation cycles at C/10. The C6_SS|LFP_SS CR2032 full cell was galvanostatically cycled at C/3 rate (1C = 170 mA g_{cat}^{-1}) in the 0.5 – 4.2 voltage range after two initial activation cycles at C/10. CV and EIS were carried out by using a VMP-3 multichannel electrochemical workstation with an integrated frequency response analyzer (Bio-Logic), while the cycling tests were performed by using a BCS-805 battery tester (Bio-Logic).

2.4. Single layer pouch (SLP) cell assembly and testing

The SLP electrodes stacking was performed in a dry room with a dew point lower than -40°C (Il Disgelo S.r.l., Torino) by using dried self-standing graphite anode and LFP cathode. The anode and cathode layers were cut in the dimensions 5.8 × 4.5 cm^2 and 5.7 × 4.4 cm^2, respectively, by a manual MTI puncher (MTI Corporation, USA). Celgard H1612 was used as separator (Celgard, Asahi Kasei Group). The electrolyte filling was performed in an Ar-filled glovebox MBraun LabMaster Pro (M. Braun Inertgas-Systeme GmbH, Germany). The electrolyte was 1 M $LiPF_6$ in ethylene carbonate (EC):dimethylcarbonate (DMC) 1:1 vol. (Solvionic, France). An OCV period of 24 h was used before cycling the SLP cell, which was cycled at the constant current of 0.5 mA in the 0.5 – 4.2 V voltage range using an N/P ratio of 1.1. The cycling test was performed using a Bio-Logic battery tester at room temperature (T = 25°C).

3. Results and discussion

The morphological and structural characterization of the self-standing electrodes (see **Figure S1** for photographic images) has been performed by SEM, EDS, and XRD. The main results are reported in Fig. 1. The SEM images at various magnification for C6_SS (Fig. 1**a-c**) indicate the presence of flake-like particles with a smooth and uniform surface, as confirmed by the SEM micrographs of the KS15 graphite powder reported in **Figure S2a,b**. Therefore, the morphology of the C6_SS electrode, compared with already reported results for graphite electrodes, suggests its suitability for application in Li-ion batteries [33]. Furthermore, the EDS mapping of C (Fig. 1**d**) and F (Fig. 1**e**) reveals homogeneous distribution of carbon and fluorine, derived from PVdF binder, without the presence of impurities. Analogously, the SEM images at different magnification of LFP_SS (Fig. 1**f-h**) reveal the expected submicrometric primary particles of LFP aggregated into micrometric secondary particles, homogeneously blended into the electrode film. The submicrometric primary particles morphology reflects the LFP powder morphology reported in **Figure S2c,d**. The agglomeration of submicrometric primary particles for olivine cathode materials can ensure a short diffusion pathway for Li^+ ions and limited side reaction with the electrolyte, as already reported [34]. Moreover, the EDS mapping of C (Fig. 1**i**), O (Fig. 1**j**), P (Fig. 1**k**), and Fe (Fig. 1**l**) of the self-standing electrode reveals homogeneous distribution of the various elements without impurities. The experimental XRD patterns of C6_SS and LFP_SS are reported in Fig. 1**m** and Fig. 1**n**, respectively, compared with the reference diffractograms for graphite (ICSD #53781) [35] and $LiFePO_4$ (ICSD #290336) [36]. The images show indexable crystalline structures

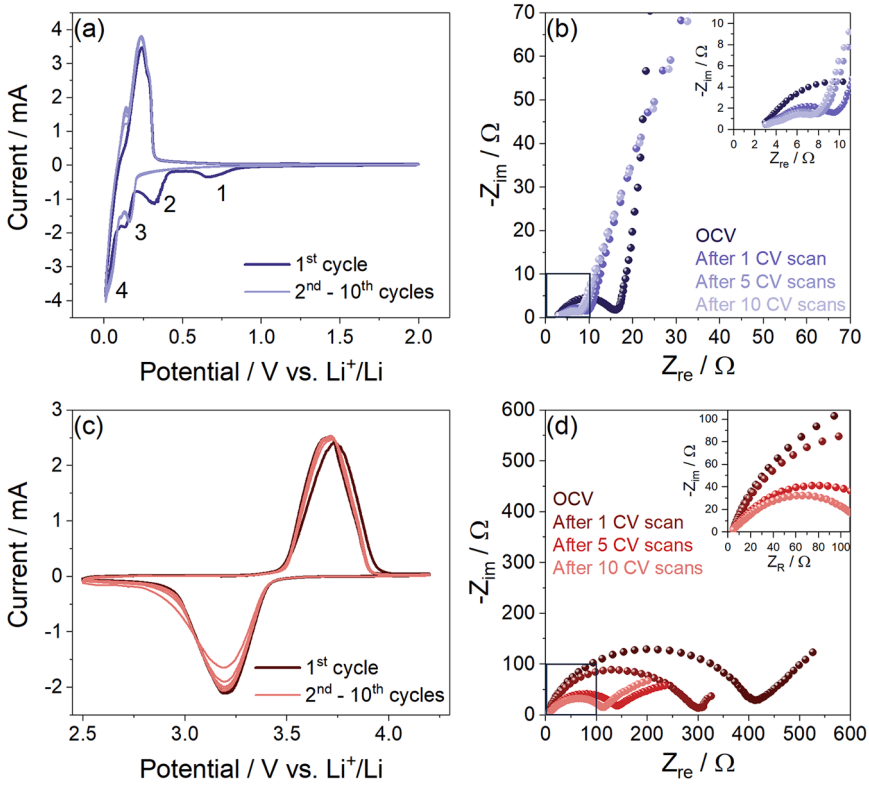

Fig. 2. **(a, c)** CV and **(b, d)** EIS measurement performed on **(a, b)** Li|C6_SS and **(c, d)** Li|LFP_SS cells. CV potential ranges 0.01 – 2 V vs. Li^+/Li and 2.5 – 4.2 V vs. Li^+/Li for C6_SS and LFP_SS, respectively; scan rate 0.1 mV s^{-1}. EIS performed at the OCV of the cells and after 1, 5, and 10 CV scans (inset reports magnification in the middle-high frequency region); frequency range 200 kHz – 100 mHz; alternate voltage signal amplitude 10 mV. T = 25°C.

Table 1
NLLS analysis of the Nyquist plots reported in Fig. 2b obtained by performing EIS on a Li|C6_SS cell. NLLS analysis were carried out through a Boukamp software and only fits with a χ^2 value of the order of 10^{-4} or lower were considered [31, 32].

Cell condition	Equivalent circuit	R_1 (Ω)	R_2 (Ω)	$R_i = R_1 + R_2$ (Ω)	χ^2
OCV	$R_e(R_1Q_1)(R_2Q_2)Q_g$	7.8 ± 0.7	7.7 ± 0.4	15.5 ± 0.8	1×10^{-5}
After 1 cycle	$R_e(R_1Q_1)(R_2Q_2)Q_g$	1.1 ± 0.2	6.0 ± 0.2	7.1 ± 0.3	5×10^{-5}
After 5 cycles	$R_e(R_1Q_1)(R_2Q_2)Q_g$	1.6 ± 0.3	4.2 ± 0.2	5.8 ± 0.4	3×10^{-5}
After 10 cycles	$R_e(R_1Q_1)(R_2Q_2)Q_g$	1.9 ± 0.2	3.3 ± 0.2	5.2 ± 0.3	2×10^{-5}

for both samples without the presence of any impurities, as confirmed by EDS analysis and by the diffractograms of KS15 and LFP powders reported in **Figure S3a** and **Figure S3b**, respectively. In summary, both structural and morphological features of C6_SS and LFP_SS electrodes indicate their possible application in energy storage devices [33,37].

The electrochemical behavior of C6_SS and LFP_SS electrodes has been investigated in lithium half-cells by combining CV and EIS measurements, as reported in Fig. 2.

The CV response of C6_SS depicted in Fig. 2**a** reveals four peaks during the first cathodic scan at 0.65 V vs. Li^+/Li (peak 1), 0.35 vs. Li^+/Li (peak 2), 0.14 vs. Li^+/Li (peak 3), and 0.02 vs. Li^+/Li (peak 4). Peaks 1 and 2 correspond to the irreversible electrolyte decomposition to form a solid electrolyte interphase (SEI) film on the electrode surface, mainly ascribed to the reduction of the carbonate solvents composing the electrolyte solution [38]. However, peaks 3 and 4 are ascribed to the typical, reversible stage intercalation process of Li^+ into graphite. Furthermore, the subsequent CV profiles suggest a remarkable reversibility of the redox processes related to peaks 3 and 4, modest polarization, and a relatively fast kinetics of the Li^+ (de-)intercalation [39]. To further investigate the stability of the SEI formation on C6_SS electrodes, EIS measurements were performed at the OCV condition of the cell as well as after 1, 5, and 10 CV cycles at the bias potential of 2.0 V vs. Li^+/Li. The corresponding Nyquist plots are reported in Fig. 2**b**. The shape of the Nyquist plots reflect the blocking-electrode behavior expected by the different states of charge of the cell at which EIS have been collected, characterized by the presence of a medium-high frequency semicircle accounting for the interface, and a low-frequency tilted line representing the cell geometrical capacity. Therefore, the impedance spectra may be represented by the equivalent circuit $R_e(R_iQ_i)Q_g$, including in series the electrolyte resistance (R_e), one or two constant phase/resistance elements (R_iQ_i) mainly accounting for the SEI formed at the electrodes, and a constant phase element related to the cell capacitance (Q_g) at the low-frequency end [31,32]. Table 1 reports the calculated resistance values, as calculated by non-linear least squares (NLLS) fits of the impedance data [31,32]. Low overall values of the total interface resistance (R_i), which decreases from about 15.5 Ω at the OCV to about 5.2 Ω after 10 CV scans, are reported, suggesting the formation of a stable SEI on the electrode surface. This is the signature of a progressive improvement of the electrode/electrolyte interface, which thus may favor the reaction kinetics [38,40]. Additionally, the overall low resistance values obtained for C6_SS also suggests a good wettability and conductivity of the electrode.

The CV response of LFP_SS is shown in Fig. 2**c**, indicating the occurrence of an oxidation process revealed by peak centered at about 3.7 V vs. Li^+/Li during the anodic scan, which is almost completely reversed into a reduction peak at about 3.2 V vs. Li^+/Li during cathodic scan, with the total (de-)insertion process ascribed to the Fe^{3+}/Fe^{2+} redox couple. It is worth noting that the CV profiles exhibit a high polarization, probably related to the higher resistivity of the self-standing LFP_SS electrode compared to a typical one adopting Al current collector

Table 2
NLLS analysis of the Nyquist plots reported in Fig. 2d obtained by performing EIS on a Li|LFP_SS cell. NLLS analysis were performed through a Boukamp software and only fits with a χ^2 value of the order of 10^{-4} or lower were considered [31,32].

Cell condition	Equivalent circuit	R_1 (Ω)	R_2 (Ω)	$R_i = R_1 + R_2$ (Ω)	χ^2
OCV	$R_e(R_1Q_1)Q_g$	391 ± 4	/	391 ± 4	5×10^{-4}
After 1 cycle	$R_e(R_1Q_1)(R_2Q_2)Q_g$	81 ± 3	212 ± 2	293 ± 4	1×10^{-4}
After 5 cycles	$R_e(R_1Q_1)(R_2Q_2)Q_g$	29 ± 2	98 ± 2	127 ± 3	1×10^{-4}
After 10 cycles	$R_e(R_1Q_1)(R_2Q_2)Q_g$	19 ± 1	90 ± 1	109 ± 1	4×10^{-5}

[41,42]. This behavior is more evidenced for LFP cathode with respect to graphite anode, due to the particularly lower conductivity of the former [42]. The high polarization could also be related to the high thickness of electrodes (110 μm) related to their high areal loading (~ 11 mg cm^{-2}), probably causing a slow complete wettability of the electrodes [43]. Nevertheless, the good reversibility of the process suggests, also in this case, a relatively fast Li^+ (de-)insertion kinetics in the olivine lattice [44]. It is worth noting that the first cycle in Fig. 2**c** is slightly different compared to the subsequent ones, indicating also for the positive electrode the formation of a suitable passivation layer on the electrode surface. To clarify this aspect, Fig. 2**d** shows the EIS measurements conducted on LFP_SS electrode in the same conditions already described for C6_SS. Analogously to C6_SS, the Nyquist plots generally reflect the blocking-electrode behavior expected for the fully-discharged state of the cell (i.e., at about 3 V vs. Li^+/Li at the OCV, and at 2.5 V vs. Li^+/Li after the CV scans) upon which the EIS have been collected, and can be represented by the same equivalent circuit already described ($R_e(R_iQ_i)Q_g$) [31,32]. Table 2 reports the interface resistance values obtained by NLLS analysis [31,32], revealing high interface resistance values, related with the already described high resistivity of the LFP_SS configuration. Nevertheless, R_i values decrease from about 391 Ω at the OCV to about 109 Ω after 10 CV cycles, suggesting also in this case the formation of a suitable and stable passivation layer at the electrode/electrolyte interface, which may favor the reaction kinetics [45], in addition to a contribution from the progressive electrode wetting, particularly relevant for the thicker LFP_SS cathode.

To investigate the ion transport properties of LFP and graphite in the self-standing configuration, the Li^+ ion diffusion coefficients were calculated through the Randles-Sevcik method [46]. Fig. 3 shows the CV responses at different scan rates of C6_SS (Fig. 3**a**) and LFP_SS (Fig. 3**c**). The values of the peak current (I_p) related to the electrochemical features of the two materials increase by increasing the scan rate (ν), following a linear trend of I_p vs. $\nu^{1/2}$, as confirmed by coefficient of determination (R^2), thus suggesting lithium diffusion as the rate-determining step of the redox processes (see **Figure S4** and **Figure S5** for the related plots for C6_SS and LFP_SS, respectively). The obtained values of the slope ($dI_p/d\nu^{1/2}$) have been used to determine the Li^+ diffusion coefficients D_{CV} ($cm^2\ s^{-1}$) for C6_SS and LFP_SS, according to the Randles-Sevcick equation (Eq. (1)) [46]:

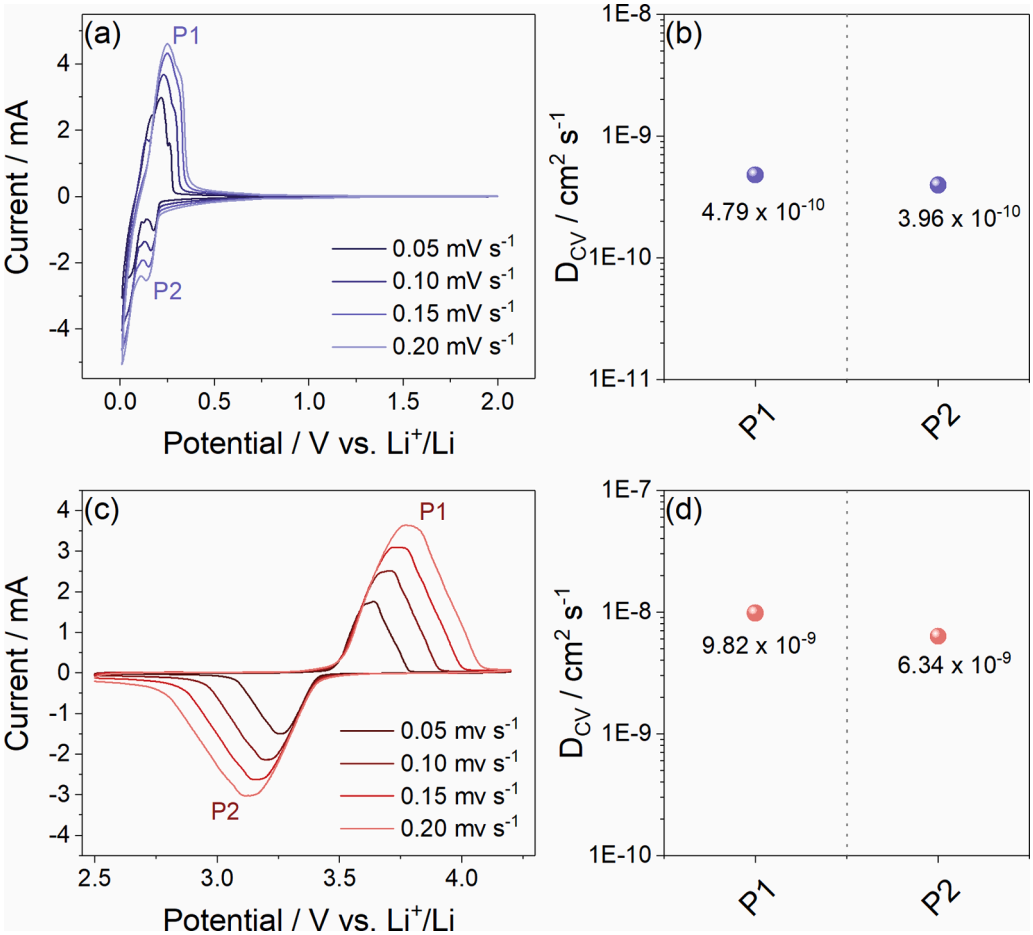

Fig. 3. Steady-state CV profiles with indexed peaks of **(a)** Li|C6_SS and **(c)** Li|LFP_SS cells at scan rates (ν) of 0.05, 0.1, 0.15, and 0.2 mV s^{-1} in the 0.01 – 2 V vs. Li^+/Li and 2.5 – 4.2 V vs. Li^+/Li potential ranges, respectively. Trend of D_{CV} at various SoC for Li^+ in **(b)** C6_SS and **(d)** LFP_SS calculated using Eq. (1), considering the linear trends reported in Figure S4 and Figure S5 (Supporting Information), respectively. T = 25°C.

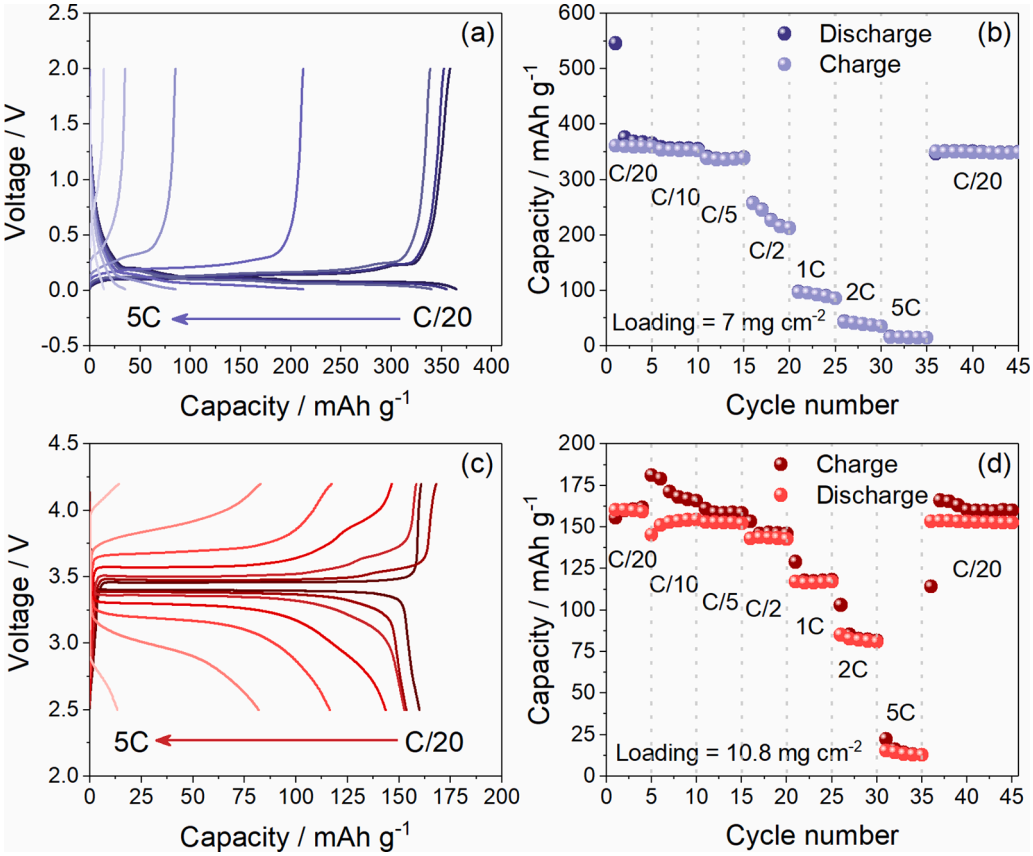

Fig. 4. Rate Capability tests of (a, b) Li|C6_SS and (c, d) Li|LFP_SS cells in terms of (a, c) voltage profiles and (b, d) corresponding cycling trend performed at C/20, C/10, C/5, C/2, 1C, 2C, and 5C currents (1C = 372 mA g^{-1} for C6_SS and 1C = 170 mA g^{-1} for LFP_SS). Voltage ranges 0.01 – 2.0 V and 2.5 – 4.2 V for C6_SS and LFP_SS, respectively. T = 25°C.

$$I_p = 0.4463zFAC\sqrt{\frac{zF\nu D_{CV}}{RT}} = 2.686x10^5AC\sqrt{z^3\nu D_{CV}} \text{ with T} = 298.15 \text{ K} \quad (1)$$

where I_p is the peak current value (A), $z = 1$ is the number of exchanged electrons for both materials [47,48], F is the Faraday constant (96485 C mol^{-1}), A is the electrodes geometric area (1.13 cm^2), C is the Li^+ concentration within the olivine or the graphite bulk (mol cm^{-3}), ν is the scan rate (V s^{-1}), R is the gas constant (8.314 J K^{-1} mol^{-1}), and T is the temperature (K). The values of D_{CV} for C6_SS and LFP_SS, as calculated by considering the I_p vs. $\nu^{1/2}$ linear slope of the current peaks ascribed to lithium intercalation into graphite and to the Fe^{3+}/Fe^{2+} redox couple, during anodic and cathodic scans, are reported in Fig. 3**b** and Fig. 3**d**, respectively. The obtained results for C6_SS (Fig. 3**b**) reveal for graphite D_{CV} values of about 10^{-10} cm^2 s^{-1} for the considered peaks, comparable with the ones obtained in other literature works [47–49]. Similarly, LFP_SS (Fig. 3**d**) shows D_{CV} values of about 10^{-9} cm^2 s^{-1}, which are also in this case in accordance with the ones reported in several literature works [50,51]. Overall, as expected, the self-standing configuration does not affect the Li^+ ion transport into LFP and graphite bulk, suggesting good diffusion features of the obtained electrodes.

The electrochemical performance of C6_SS and LFP_SS in lithium half-cells subjected to galvanostatic cycling are reported in Fig. 4 and Fig. 5. The rate capability of both materials (Fig. 4) is evaluated in terms of voltage profiles (Fig. 4**a** and Fig. 4**c** for C6_SS and LFP_SS, respectively) and specific capacity (Fig. 4**b** and Fig. 4**d** for C6_SS and LFP_SS, respectively), by increasing the current from C/20 to 5C (1C = 372 mA g^{-1} for C6_SS and 1C = 170 mA g^{-1} for LFP_SS). The cells show the expected shape of the voltage profiles at the various C-rates for both materials, characterized by the typical stage (de-)intercalation of lithium in graphite for C6_SS (Fig. 4**a**) and by the presence of a plateau at an average voltage of 3.45 V, ascribed to Fe^{3+}/Fe^{2+} redox couple, for LFP_SS (Fig. 4**c**), in agreement with CVs in Fig. 2**a** and Fig. 2**c**, respectively. Furthermore, the voltage profiles evidence an increase of polarization by raising the current, which leads to the decrease of the capacity of the two electrodes from 360 mAh g^{-1} (i.e. 97 % of the theoretical value) and 160 mAh g^{-1} (i.e. 94 % of the theoretical value) at C/20 for C6_SS and LFP_SS, respectively, to about 15 mAh g^{-1} for both materials (i.e. 4 % of the theoretical value for the former and 9 % for the latter) at 5C, as indeed expected by the increase of the ohmic polarization. On the other hand, the capacity trends of C6_SS (Fig. 4**b**) and LFP_SS (Fig. 4**d**) reveal that the initial capacities are recovered for both electrodes by decreasing back the current to C/20, thus suggesting a good capacity retention and stability of the self-standing electrodes upon the stress caused by increasing the current [52]. It is worth noting that for LFP_SS the coulombic efficiency is low at lower currents (see Fig. 4**d**), probably related to the occurrence of parasitic reactions in the cell, especially relevant at low current rates. However, this issue seems to not affect the performance of LFP_SS at higher currents, revealing higher coulombic efficiencies.

The stability of the electrochemical lithium (de-)intercalation process of C6_SS and (de-insertion) process of LFP_SS in half-cell has been further investigated by repeated charge/discharge cycles at a constant C-rate of C/3. The corresponding capacity values are shown in Fig. 5. This current rate has been chosen for both electrodes according to the rate capability test results, where C/3 appeared to guarantee both a relatively high capacity for the C6_SS electrode and a relatively high coulombic efficiency for the LFP_SS one, avoiding the described possible side effects (two preliminary cycles at C/10 current had been carried out to allow the formation of a suitable SEI at the electrode/electrolyte

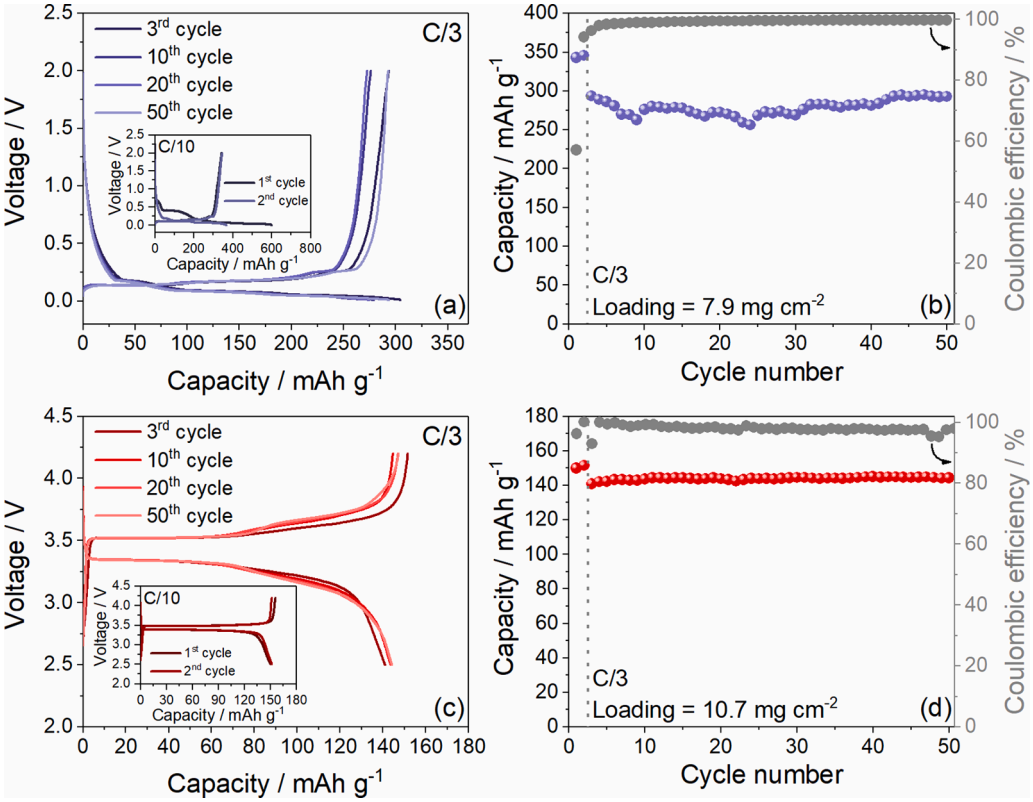

Fig. 5. Galvanostatic cycling performance of **(a, b)** Li|C6_SS and **(c, d)** Li|LFP_SS cells at the constant current rate of C/3 (1C = 372 mA g^{-1} for C6_SS and 1C = 170 mA g^{-1} for LFP_SS), after 2 activation cycle at C/10, in terms of **(a, c)** voltage profiles and **(b, d)** corresponding cycling trend with discharge capacity in left-hand side *y*-axis and coulombic efficiency in right-hand side *y*-axis (inset shows the profiles of the 2 activation cycles). Voltage ranges 0.01 – 2.0 V and 2.5 – 4.2 V for C6_SS and LFP_SS, respectively. T = 25°C.

interface of the electrodes) [40,45]. The voltage profiles of the tests performed on C6_SS (Fig. 5**a**) and LFP_SS (Fig. 5**c**) show the well-defined behaviors already described, with a maximum capacity of about 295 mAh g^{-1} for the former and 140 mAh g^{-1} for the latter after the activation cycles, in full agreement with the rate capability tests. It is worth noting that the irreversible formation of the SEI at the first cycle on C6_SS electrode (see inset of Fig. 5**a**) is in agreement with the result observed during CV test (see Fig. 2**a**). The C6_SS cell (Fig. 5**b**) reveals a coulombic efficiency of 57 % at the first cycle, related to the already described SEI formation, which increases and ranges from about 99 % to 100 % during the subsequent ones, with a slightly oscillation of the capacity values probably related to minor temperature oscillations during the test, which affect the intercalation kinetics of the material. Moreover, the LFP_SS cell (Fig. 5**d**) shows a coulombic efficiency of 95 % at the first cycle, which increases and ranges from 97 % to 99 % during the subsequent ones, with a remarkable capacity retention. Relevantly, the obtained results reveal the expected high stability of the olivine structure [42], associated with good capacity values and high coulombic efficiency for both electrodes, mandatory features for the possible application in a Li-ion system [53], thus suggesting the suitability of C6_SS and LFP_SS as candidate electrodes for application in enhanced energy density systems [6].

In this regards, Fig. 6 reports the electrochemical performance of a C6_SS|LFP_SS coin-type full cell at the constant current rate of C/3 as referred to the cathode active material mass (1C = 170 mA g_{cat}^{-1}), after two activation cycles at C/10, with a negative to positive capacity ratio (N/P) of 1.1. The voltage profiles of Fig. 6**a** reflect the combination of the respective anode and cathode signatures. In particular, the profile of the first cycle (see inset in Fig. 6**a**) evidences the formation of the SEI layer at the electrodes surface, while all the cycles are characterized by a voltage plateau at about 3.3 V ascribed to Fe^{3+}/Fe^{2+} redox couple. Furthermore, the profiles reveal a maximum capacity of about 130 mAh g_{cat}^{-1}, in line with the data obtained for the half-cells (see Fig. 5**d**). The cycling trend reported in Fig. 6**b** shows a good stability of the cell, which exhibits a coulombic efficiency of 76 % at the first cycle, due to the abovementioned SEI formation, which raises and reaches 99 % after 15 cycles, as depicted by the magnification of the coulombic efficiency values represented in Fig. 6**c**. Particularly, after initial cycles, the cell possesses very high coulombic efficiency values approaching 99.5 % for all the measurements, key parameter for the stability of the device [54]. Furthermore, the cell exhibits a capacity retention of 70 % after 150 cycles and of 56 % after 300 cycles, which could be related to the high loading of the electrodes adopted, which present an areal capacity of about 1.5 mAh cm^{-2}. Indeed, high areal capacities coupled with satisfactory cycling stability are important for the possible scaling up of the cell prototype [6,53]. Fig. 6**d** reveals the gravimetric energy density of the cell calculated by integrating the capacity as a function of the cell voltage for selected cycles, normalized to the total mass of the self-standing electrodes (anode + cathode), compared to the energy density values predicted by adding to the same electrodes the weight of Al (MTI Corp., 20 μm thickness, 6.24 mg for 1.13 cm^2 disk) and Cu (MTI Corp., 15 μm thickness, 9.68 mg for 1.13 cm^2 disk) current collectors. The cell reveals high initial gravimetric energy density for the self-standing configuration (240 Wh Kg_{an+cat}^{-1}), which decreases as the cycles progress, due to the associated capacity fading, while maintaining values over 130 Wh Kg_{an+cat}^{-1} after 300 cycles. It is worth noting that the same electrodes, if coated onto Al and Cu current collectors, would reveal lower energy densities, as expected by the increase of the cell weight. Although, the gravimetric energy density of the entire cell, either with self-standing electrodes or with additional current collectors, should be lower as the contribution of other components (e.g. electrolyte, separator, cell casing) on the total weight is not considered here

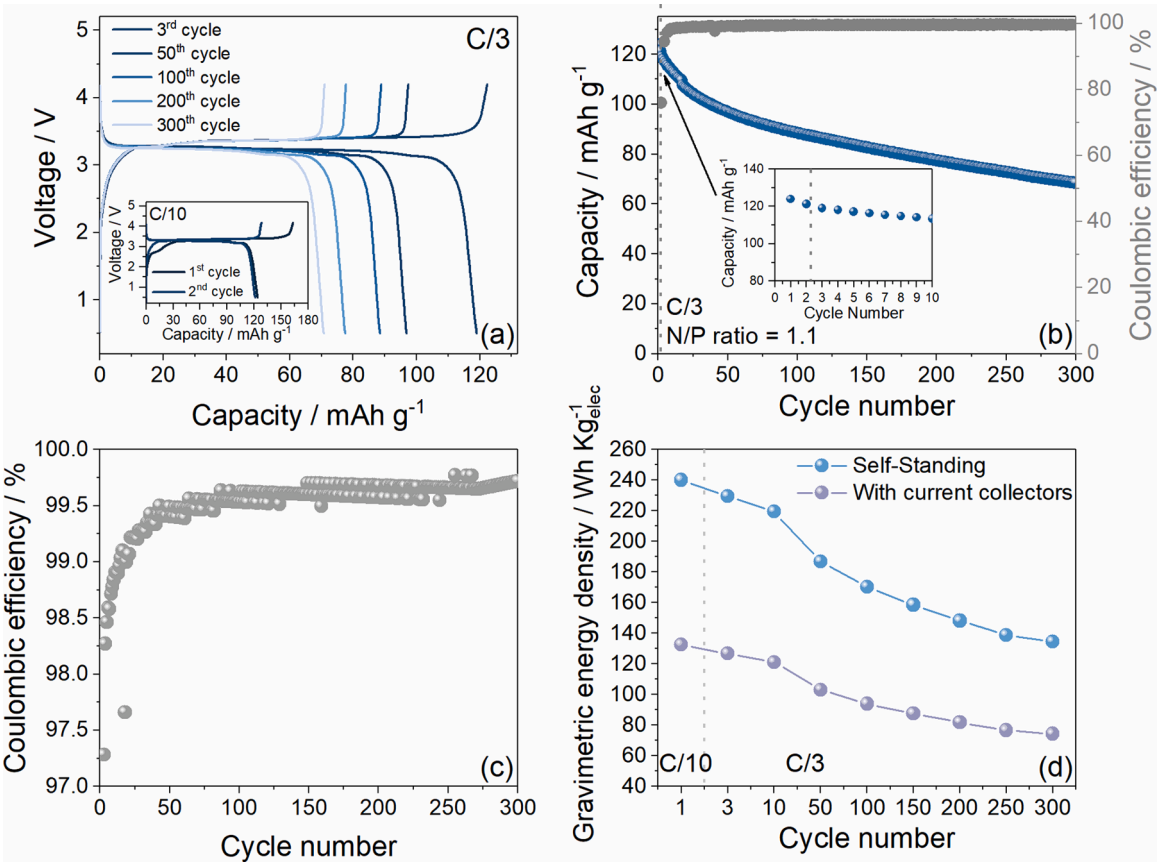

Fig. 6. Galvanostatic cycling performance of the C6_SS|LFP_SS full cell at the constant current rate of C/3 (1C = 170 mA g_{cat}^{-1}), after 2 activation cycle at C/10, in terms of (a) voltage profiles and (b) cycling trend with discharge capacity in left-hand side y-axis and coulombic efficiency in right-hand side y-axis (insets of panels (a) and (b) show the profiles of the 2 activation cycles and a magnification of the first 10 cycles trend, respectively). (c) Magnified cycling trend of coulombic efficiency. (d) Trends of calculated gravimetric energy density for selected cycles considering the mass of the Self-Standing electrodes and including the mass of Al and Cu current collectors. T = 25°C.

[55]. The obtained results for the full cell configuration based on self-standing electrodes, especially the one related to the gravimetric energy density, are promising for its possible application in higher energy density devices, such as portable electronic devices (i.e. smartwatches). Particularly, the energy density obtained in this work is similar to other achieved in literature with $LiMn_{0.7}Fe_{0.3}PO_4$ as positive electrode material [17], or in free-standing configuration coupled with Li metal for LFP [56]. Furthermore, the achieved energy density for the C6_SS|LFP_SS cell is also comparable with the ones obtained in configurations employing cathodes with higher working potential (i.e. $LiCoO_2$, $LiNi_{0.8}Mn_{0.1}Co_{0.1}O_2$) [57,58], confirming the improved performance of the self-standing configuration also compared with higher energy density systems.

As already mentioned, the promising results obtained in coin-cell configuration suggest the application of the self-standing electrodes in commercial batteries for portable electronic devices. Moreover, these results may suggest a possible upscaling of the cell format to single layer pouch (SLP) cells or cylindrical cells. Indeed, the evaluation of the compatibility of the self-standing electrodes in a proof-of-concept SLP cell is evaluated in **Figure S6**, Supporting Information. **Figures S6a** and **S6b** reveal the photographic images of the LFP_SS electrode and of the final SLP cell, respectively. **Figure S6c** reports the electrochemical response of the SLP cell cycled at the constant current of 0.5 mA with an N/P ratio of 1.1. The cycling trend reveals an initial capacity of about 10 mAh (~ 60 mAh g^{-1}), which decreases reaching a final value of about 2.5 mAh (~ 20 mAh g^{-1}) after 20 cycles, and a coulombic efficiency of about 95 % after the initial cycles. Furthermore, the voltage profile of the second cycle in the inset of **Figure S6c** shows the same shape described above for full coin cell, with the presence of the combined features of anode and cathode, respectively (see Fig. 6**a**). These results suggest a partial operation of the LFP cathode, which limits the capacity of the cell, as well as possible parasitic reaction and gas evolution inside the cell after initial cycles, reflected in the poor cycle life and coulombic efficiency [59]. As already mentioned, the LFP_SS and C6_SS electrodes have been prepared without the use of any plasticizer other than PVdF binder, thus the electrodes presented reduced mechanical properties that may limit their application in industrial cell formats, especially cylindrical cells [27,60]. Overall, the proof-of-concept SLP cell evidences the compatibility of the self-standing electrodes in upscaled batteries, despite further optimization are needed to improve the performance. Indeed, these achievements, especially the one obtained in coin-type full cell, lead to the possibility of using this cell design to further decrease the raw materials cost and weight of commercial batteries, enhancing at the same time the achievable energy density and intrinsic safety.

4. Conclusions

In the present study we evaluated the use of an easy technique to produce self-standing electrodes for application in a new design graphite|LFP Li-ion full cell with enhanced energy density and lower cost. The produced C6_SS and LFP_SS electrodes presented the expected morphology and structure, also compared with the commercial material powders, suitable for application in lithium cells. The investigation of the electrochemical process by CV revealed the expected reversible peaks of the Fe^{3+}/Fe^{2+} redox couple for LFP_SS and the irreversible

peaks related to SEI formation coupled with the reversible stage lithium (de-)intercalation for C6_SS, with high polarization for the former ascribed to the higher resistivity of the electrode without the current collector. EIS measurements carried out upon CV confirmed the lower conductivity of the LFP_SS electrode, however with a decrease of the interfacial resistance upon cycling for both LFP_SS and C6_SS, suggesting the formation of stable electrode/electrolyte interfaces on the electrodes surface. The diffusion properties of the self-standing electrodes studied by CV revealed values comparable with the literature, confirming good lithium ion diffusion. The test in lithium half-cells showed satisfactory rate capability from C/20 to 5C for both samples with a maximum capacity of about 360 mAh g^{-1} and 160 mAh g^{-1} for C6_SS and LFP_SS, respectively, with a good capacity retention at C/3 current. The C6_SS|LFP_SS full cell with the N/P ratio of 1.1 cycled at the constant current rate of C/3 (1C = 170 mA g_{cat}^{-1}) revealed a capacity of about 120 mAh g_{cat}^{-1}, suitable capacity retention of about 56 % after 300 cycles, very high coulombic efficiency approaching 99.5 % and an initial energy density of about 240 Wh Kg_{an+cat}^{-1}. The proof-of-concept SLP cell shows the compatibility of the self-standing configuration in upscaled devices, despite further optimizations are needed. In particular, the energy density values obtained for the cell assembled with self-standing electrodes, compared with several literature results, are promising for the possible implementation of this configuration in low cost and high energy density devices, avoiding the use of Cu and Al current collectors.

CRediT authorship contribution statement

Luca Minnetti: Writing – original draft, Visualization, Methodology, Investigation, Formal analysis, Data curation, Conceptualization, Writing – review & editing. **Leonardo Sbrascini:** Writing – original draft, Visualization, Methodology, Investigation, Formal analysis, Data curation. **Asia Patriarchi:** Visualization, Methodology, Investigation, Formal analysis. **Antunes Staffolani:** Writing – review & editing, Visualization, Methodology, Investigation, Formal analysis, Conceptualization. **Maddalena Barcaioni:** Visualization, Methodology, Investigation, Formal analysis. **Luca Bottoni:** Visualization, Methodology, Investigation, Formal analysis. **Francesco Nobili:** Writing – review & editing, Validation, Supervision, Funding acquisition, Conceptualization.

Declaration of competing interest

The authors declare that they have no known competing financial interests or personal relationships that could have appeared to influence the work reported in this paper.

Acknowledgements

This work was financially supported by MUR – PNRR (Decreto Direttoriale n. 703 del 20–4-2022), within the framework of the project "VITALITY - Innovation, digitalisation and sustainability for the diffused economy in Central Italy" (cod. ECS_00000041), Spoke 9 - Nanostructured materials and devices and was also carried out within the MOST e Sustainable Mobility Center and received funding from the European Union Next-GenerationEU (PIANO NAZIONALE DI RIPRESA E RESILIENZA (PNRR) e MISSIONE 4 COMPONENTE 2, INVESTIMENTO 1.4 e D.D. 1033 17/06/2022, CN00000023). This manuscript reflects only the authors' views and opinions, neither the European Union nor the European Commission can be considered responsible for them.

Supplementary materials

Supplementary material associated with this article can be found, in the online version, at doi:10.1016/j.electacta.2025.146806.

Data availability

Data will be made available on request.

References

[1] B. Li, X. Gao, J. Li, C. Yuan, Life Cycle Environmental Impact of High-Capacity Lithium Ion Battery with Silicon Nanowires Anode for Electric Vehicles, Environ. Sci. Technol. 48 (2014) 3047–3055.
[2] M. Armand, J.-M. Tarascon, Building better batteries, Nature 451 (2008) 652–657.
[3] F. Duffner, M. Wentker, M. Greenwood, J. Leker, Battery cost modeling: A review and directions for future research, Renew. Sustain. Energy Rev. 127 (2020) 109872.
[4] D. Larcher, J.M. Tarascon, Towards greener and more sustainable batteries for electrical energy storage, Nat. Chem. 7 (2015) 19–29.
[5] W. Yourey, Cell Design Considerations and Impact on Energy Density—A Practical Approach to EV Cell Design, World Electric Vehicle Journal 14 (2023) 279.
[6] M.J. Lain, J. Brandon, E. Kendrick, Design Strategies for High Power vs. High Energy Lithium Ion Cells, Batteries 5 (2019) 64.
[7] B. Scrosati, J. Hassoun, Y.K. Sun, Lithium-ion batteries. A look into the future, Energy Environ. Sci. 4 (2011) 3287–3295.
[8] M. Wentker, M. Greenwood, J. Leker, A Bottom-Up Approach to Lithium-Ion Battery Cost Modeling with a Focus on Cathode Active Materials, Energies (Basel) 12 (2019) 504.
[9] F. Schipper, D. Aurbach, A brief review: Past, present and future of lithium ion batteries, Russ. J. Electrochem. 52 (2016) 1095–1121.
[10] A. Yamada, M. Hosoya, S.C. Chung, Y. Kudo, K. Hinokuma, K.Y. Liu, Y. Nishi, Olivine-type cathodes: Achievements and problems, J. Power Sources 119-121 (2003) 232–238.
[11] W. Wan, H. Wang, Study on the First-Principles Calculations of Graphite Intercalated by Alkali Metal (Li, Na, K), Int. J. Electrochem. Sci. 10 (2015) 3177–3184.
[12] K. Nobuhara, H. Nakayama, M. Nose, S. Nakanishi, H. Iba, First-principles study of alkali metal-graphite intercalation compounds, J. Power Sources 243 (2013) 585–587.
[13] A.Franco Gonzalez, N.-H. Yang, R.-S. Liu, Silicon Anode Design for Lithium-Ion Batteries: Progress and Perspectives, J. Phys. Chem. C 121 (2017) 27775–27787.
[14] B. Zhu, X. Wang, P. Yao, J. Li, J. Zhu, Towards high energy density lithium battery anodes: silicon and lithium, Chem. Sci. 10 (2019) 7132–7148.
[15] J.T. Frith, M.J. Lacey, U. Ulissi, A non-academic perspective on the future of lithium-based batteries, Nat. Commun. 14 (2023) 420.
[16] F.M.N.U. Khan, M.G. Rasul, A.S.M. Sayem, N.K. Mandal, Design and optimization of lithium-ion battery as an efficient energy storage device for electric vehicles: A comprehensive review, J. Energy Storage 71 (2023) 108033.
[17] L. Minnetti, F.M. Maddar, A.K. Haridas, M. Capener, F. Nobili, I. Hasa, Assessing Manufacturing-Performance Correlation On $LiMn_{0.7}Fe_{0.3}PO_4$ Electrodes For Application In Upscaled Li-Ion Battery Cells, Batteries Supercaps 8 (2025) e202400645.
[18] I. Hasa, S. Passerini, K. Edstrom, P. Stevens, A. Romanello, R. Scipioni, E. Sheridan, Ensuring accurate Key Performance Indicators for Battery applications by implementing consistent Reporting Methodologies, Transp. Res. Procedia 72 (2023) 3625–3632.
[19] H. Zheng, J. Li, X. Song, G. Liu, V.S. Battaglia, A comprehensive understanding of electrode thickness effects on the electrochemical performances of Li-ion battery cathodes, Electrochim. Acta 71 (2012) 258–265.
[20] B. Zhou, A. Bonakdarpour, I. Stoševski, B. Fang, D.P. Wilkinson, Modification of Cu current collectors for lithium metal batteries – A review, Prog. Mater. Sci. 130 (2022) 100996.
[21] H. Abe, M. Kubota, M. Nemoto, Y. Masuda, Y. Tanaka, H. Munakata, K. Kanamura, High-capacity thick cathode with a porous aluminum current collector for lithium secondary batteries, J. Power Sources 334 (2016) 78–85.
[22] V. Marangon, E. Barcaro, L. Minnetti, W. Brehm, F. Bonaccorso, V. Pellegrini, J. Hassoun, Current collectors based on multiwalled carbon-nanotubes and few-layer graphene for enhancing the conversion process in scalable lithium-sulfur battery, Nano Res 16 (2023) 8433–8447.
[23] I.V. Thorat, D.E. Stephenson, N.A. Zacharias, K. Zaghib, J.N. Harb, D.R. Wheeler, Quantifying tortuosity in porous Li-ion battery materials, J. Power Sources 188 (2009) 592–600.
[24] F. Pouraghajan, H. Knight, M. Wray, B. Mazzeo, R. Subbaraman, J. Christensen, D. Wheeler, Quantifying Tortuosity of Porous Li-Ion Battery Electrodes: Comparing Polarization-Interrupt and Blocking-Electrolyte Methods, J. Electrochem. Soc. 165 (2018) A2644–A2653.
[25] C.-H. Chen, J.-M. Chiu, I. Shown, C.-H. Wang, Simple way of making free-standing cathode electrodes for flexible lithium-ion batteries, RSC Adv 12 (2022) 9249–9255.
[26] E.M.C. Jones, M.N. Silberstein, S.R. White, N.R. Sottos, In Situ Measurements of Strains in Composite Battery Electrodes during Electrochemical Cycling, Exp. Mech. 54 (2014) 971–985.
[27] I. Phiri, J. Kim, C.T. Mpupuni, K. Ssendagire, J.-T. Kim, Y. Lee, S.-Y. Ryou, Keeping it Simple: Free-Standing, Flexible Cathodic Electrodes for High Rate, Long Cycling Lithium Batteries, ACS Appl. Energy Mater. 5 (2022) 13535–13543.
[28] A. Du Pasquier, T. Zheng, G.G. Amatucci, A.S. Gozdz, Microstructure effects in plasticized electrodes based on PVDF–HFP for plastic Li-ion batteries, J. Power Sources 97–98 (2001) 758–761.

[29] R. Morasch, B. Suthar, H.A. Gasteiger, Simple Way of Making Free-Standing Battery Electrodes and their Use in Enabling Half-Cell Impedance Measurements via μ-Reference Electrode, J. Electrochem. Soc. 167 (2020) 100540.
[30] J. Wesselkämper, L. Dahrendorf, L. Mauler, S. Lux, S. von Delft, Towards circular battery supply chains: Strategies to reduce material demand and the impact on mining and recycling, Resour. Policy 95 (2024) 105160.
[31] B. Boukamp, A Nonlinear Least Squares Fit procedure for analysis of immittance data of electrochemical systems, Solid State Ion 20 (1986) 31–44.
[32] B. Boukamp, A package for impedance/admittance data analysis, Solid State Ion 18–19 (1986) 136–140.
[33] L.S. Montagna, F. de C. Fim, G.B. Galland, N.R. de S. Basso, Synthesis of Poly (propylene)/Graphite Nanocomposites by in Situ Polymerization, Macromol. Symp. 299–300 (2011) 48–56.
[34] S. Brutti, J. Hassoun, B. Scrosati, C.-Y. Lin, H. Wu, H.-W. Hsieh, A high power Sn–C/C–$LiFePO_4$ lithium ion battery, J. Power Sources 217 (2012) 72–76.
[35] J.D. Bernal, The structure of graphite, Proceedings of the Royal Society of London. Series A, Containing Papers of a Mathematical and Physical Character 106 (1924) 749–773.
[36] M. Roberts, J.J. Biendicho, S. Hull, P. Beran, T. Gustafsson, G. Svensson, K. Edström, Design of a new lithium ion battery test cell for in-situ neutron diffraction measurements, J. Power Sources 226 (2013) 249–255.
[37] Y. Wang, Y. Wang, E. Hosono, K. Wang, H. Zhou, The design of a $LiFePO_4$/carbon nanocomposite with a core-shell structure and its synthesis by an in situ polymerization restriction method, Angewandte Chemie – Int. Edition 47 (2008) 7461–7465.
[38] L. Zhao, D. Jing, Y. Shi, Q. Zhuang, Y. Cui, Z. Ju, Y. Cui, TriMethylene sulfite as a novel additive for SEI film formation in lithium-ion batteries, Ionics (Kiel) 26 (2020) 4813–4824.
[39] Y. Zhao, Y. Fu, Y. Meng, Z. Wang, J. Liu, X. Gong, Challenges and strategies of lithium-ion mass transfer in natural graphite anode, Chem. Eng. J. 480 (2024) 148047.
[40] K. Xu, Electrolytes and interphases in Li-ion batteries and beyond, Chem. Rev. 114 (2014) 11503–11618.
[41] G. Apachitei, M. Hidalgo, D. Dogaru, M. Lain, R. Heymer, J. Marco, M. Copley, Optimisation of Industrially Relevant Electrode Formulations for LFP Cathodes in Lithium Ion Cells, Batteries 9 (2023) 192.
[42] A.K. Padhi, K.S. Nanjundaswamy, J.B. Goodenough, Phospho-olivines as Positive-Electrode Materials for Rechargeable Lithium Batteries, J. Electrochem. Soc. 144 (1997) 1188–1194.
[43] A. El Malki, M. Asch, O. Arcelus, A. Shodiev, J. Yu, A.A. Franco, Machine learning for optimal electrode wettability in lithium ion batteries, J. Power Sources Adv. 20 (2023) 100114.
[44] L. Minnetti, V. Marangon, J. Hassoun, Synthesis and Characterization of a $LiFe_{0.6}Mn_{0.4}PO_4$ Olivine Cathode for Application in a New Lithium Polymer Battery, Adv. Sustain. Syst. 6 (2022) 2100464.
[45] D. Aurbach, Review of selected electrode-solution interactions which determine the performance of Li and Li ion batteries, J. Power Sources 89 (2000) 206–218.
[46] J.E.B. Randles, Kinetics of rapid electrode reactions, Discuss. Faraday Soc. 1 (1947) 11–19.
[47] D. Aurbach, B. Markovsky, A. Shechter, Y. Ein-Eli, H. Cohen, A Comparative Study of Synthetic Graphite and Li Electrodes in Electrolyte Solutions Based on Ethylene Carbonate-Dimethyl Carbonate Mixtures, J. Electrochem. Soc. 143 (1996) 3809–3820.
[48] M.D. Levi, D. Aurbach, The mechanism of lithium intercalation in graphite film electrodes in aprotic media. Part 1. High resolution slow scan rate cyclic voltammetric studies and modeling, J. Electroanal. Chem 421 (1997) 79–88.
[49] E. Markevich, E. Pollak, G. Salitra, D. Aurbach, On the performance of graphitized meso carbon microbeads (MCMB)–meso carbon fibers (MCF) and synthetic graphite electrodes at elevated temperatures, J. Power Sources 174 (2007) 1263–1269.
[50] D. Di Lecce, J. Hassoun, Lithium Transport Properties in $LiMn_{1-\alpha}Fe_{\alpha}PO_4$ Olivine Cathodes, J. Phys. Chem. C 119 (2015) 20855–20863.
[51] B. Özdogru, H. Dykes, S. Padwal, S. Harimkar, Ö.Ö. Çapraz, Electrochemical strain evolution in iron phosphate composite cathodes during lithium and sodium ion intercalation, Electrochim. Acta 353 (2020) 136594.
[52] D. Di Lecce, J. Hassoun, Lithium Metal Battery Using $LiFe_{0.5}Mn_{0.5}PO_4$ Olivine Cathode and Pyrrolidinium-Based Ionic Liquid Electrolyte, ACS Omega 3 (2018) 8583–8588.
[53] G. Bridgewater, M.J. Capener, J. Brandon, M.J. Lain, M. Copley, E. Kendrick, A Comparison of Lithium-Ion Cell Performance across Three Different Cell Formats, Batteries 7 (2021) 38.
[54] J. Asenbauer, A. Varzi, S. Passerini, D. Bresser, Revisiting the energy efficiency and (potential) full-cell performance of lithium-ion batteries employing conversion/alloying-type negative electrodes, J. Power Sources 473 (2020) 228583.
[55] C.X. Zu, H. Li, Thermodynamic analysis on energy densities of batteries, Energy Environ. Sci. 4 (2011) 2614–2624.
[56] A. Patriarchi, H. Darjazi, L. Minnetti, L. Sbrascini, G.A. Elia, V. Castorani, M.Á. Muñoz-Márquez, F. Nobili, All-Solid-State Li-Metal Cell Using Nanocomposite TiO_2/Polymer Electrolyte and Self-Standing $LiFePO_4$ Cathode, Batteries 10 (2024) 11.
[57] Y. Zhang, H. Wang, Z. Li, X. Ge, K. Huang, J.Q. Huang, L. Huang, Z. Li, Y. Huang, Innovative Anode Design to Enhance Both Volumetric and Gravimetric Energy Densities of $LiCoO_2$||Graphite Pouch Cells, Adv. Energy Mater. 15 (2024) 2403804.
[58] J. Sharma, R. Tao, G. Polizos, N. Kanbargi, B. LaRiviere, J. Li, A lightweight and metal-free current collector for battery anode applications, J. Energy Storage 79 (2024) 110161.
[59] P.G. Balakrishnan, R. Ramesh, T.Prem Kumar, Safety mechanisms in lithium-ion batteries, J. Power Sources 155 (2006) 401–414.
[60] L.S. de Vasconcelos, R. Xu, J. Li, K. Zhao, Grid indentation analysis of mechanical properties of composite electrodes in Li-ion batteries, Extreme Mech. Lett. 9 (2016) 495–502.